arXiv:1402.6860v1 [cond-mat.quant-gas] 27 Feb 2014

Global Phase Diagram of Two-Component Bose Gases in Antiparallel Magnetic Fields

Shunsuke Furukawa and Masahito Ueda
Department of Physics, University of Tokyo, 7-3-1 Hongo, Bunkyo-ku, Tokyo 113-0033, Japan
(Dated: February 28, 2014)

We study the ground-state phase diagram of two-dimensional two-component (or pseudospin-$\frac{1}{2}$) Bose gases in antiparallel synthetic magnetic fields, in the space of the total filling factor $\nu_{\rm tot}$ and the ratio of the intercomponent coupling $g_{\uparrow\downarrow}$ to the intracomponent one $g > 0$. This time-reversal-invariant setting represents a bosonic analogue of spin Hall systems. Using exact diagonalization, we find that (fractional) quantum spin Hall states composed of two nearly independent quantum Hall states are remarkably robust and persist even when $g_{\uparrow\downarrow} \approx g$. For $g_{\uparrow\downarrow} = -g$, we obtain exact many-body ground states in which particles of different spin states form pairs. This gives the exact critical line beyond which the system collapses.

PACS numbers: 05.30.Jp, 72.25.-b, 73.43.Cd

Recent years have witnessed a rapid development in experimental techniques for creating synthetic gauge fields in ultracold atomic gases [1, 2]. By optically coupling internal states of the atoms, a nearly uniform synthetic magnetic field has been realized [3], opening up a new avenue towards the realization of quantum Hall (QH) states. Moreover, magnetic fields of antiparallel directions have been optically induced in two-component (pseudospin-$\frac{1}{2}$) Bose gases, enabling observation of a spin Hall effect arising from spin-dependent Lorentz forces [4]. There have also been proposals to realize similar gauge fields by inducing laser-assisted tunneling in tilted optical lattices [5, 6]. Although the spin Hall effect observed in Ref. [4] was still in a classical regime, the physical settings of Refs. [4–6] show striking resemblances with quantum spin Hall (QSH) systems studied in semiconductors.

The QSH effect was first studied in graphene [7] and semiconductors with a strain gradient structure [8]. It was later experimentally observed in HgTe/CdTe quantum wells [9] following a theoretical proposal [10]. A notable feature of QSH systems is that they exhibit a pair of gapless edge modes protected by time-reversal (TR) symmetry while having an excitation gap in the bulk. The simplest model of QSH systems is a pair of integer QH systems with opposite chiralities. A natural generalization is to couple a pair of fractional QH states to construct an interacting analogue of QSH states with a fractionally quantized spin Hall conductance [8]. Interacting two-component atomic gases in high antiparallel magnetic fields would provide ideal platforms for studying interplay between strong correlations and TR symmetry. While fractional QSH states would appear naturally for a strong intracomponent repulsion $g > 0$ and a weak intercomponent coupling $g_{\uparrow\downarrow}$ [11], it is interesting to ask whether they survive or are replaced by new quantum phases when $g_{\uparrow\downarrow}/g$ is increased.

In this Letter, we study pseudospin-$\frac{1}{2}$ Bose gases in high antiparallel magnetic fields. We determine the ground-state (GS) phase diagram in the space of the total filling factor $\nu_{\rm tot} = (N_\uparrow + N_\downarrow)/N_\phi$ and the ratio $g_{\uparrow\downarrow}/g$ (Fig. 1). Here, N_ϕ is the number of magnetic flux quanta piercing each component, $N_\uparrow$ ($N_\downarrow$) is the number of particles in the spin state $\uparrow$ ($\downarrow$), and we assume balanced populations $N_\uparrow = N_\downarrow$ in most of the calculations.

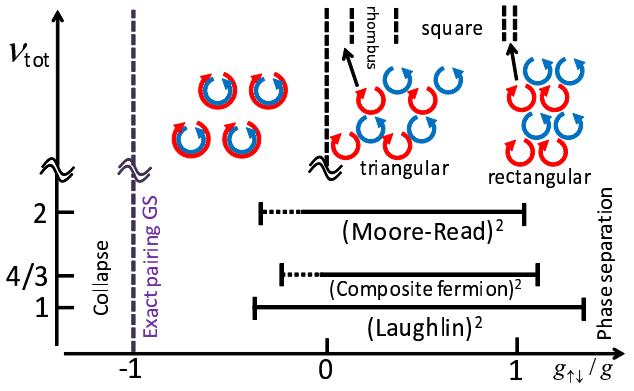

FIG. 1: (color online) Ground-state phase diagram in the space of the total filling factor $\nu_{\rm tot} = (N_\uparrow + N_\downarrow)/N_\phi$ and the ratio of the intercomponent to intracomponent coupling constants, $g_{\uparrow\downarrow}/g$. Within the Gross-Pitaevskii theory, a large-$\nu_{\rm tot}$ region shows the same vortex phase diagram as in the case of parallel magnetic fields studied previously [19, 20]. For small $\nu_{\rm tot}$, (fractional) quantum spin Hall states composed of two nearly independent quantum Hall states (Laughlin, composite fermion, and Moore-Read states), appear over certain ranges of $g_{\uparrow\downarrow}/g$. The estimates of the left boundaries of these states at $\nu_{\rm tot} = 4/3$ and 2 still involve large uncertainties as indicated by dotted lines (see the Supplemental Material [12]). On the critical line $g_{\uparrow\downarrow}/g = -1$ beyond which the system collapses, pairing states constitute the exact many-body ground states.

For $g_{\uparrow\downarrow} = 0$, the system decouples into two independent scalar Bose gases. The single-component problem in a synthetic magnetic field can be realized in a rotating gas and has been studied in a number of works [13]. For moderate magnetic fields, Abrikosov's triangular vortex lattice is formed in a Bose-Einstein condensate as observed experimentally [3, 14]. For high magnetic fields

(i.e., low filling factors $\nu = N/N_\phi$), theory predicts that the vortex lattice melts, and incompressible QH states appear at various integer and fractional $\nu(\lesssim 6)$. Examples include a bosonic Laughlin state at $\nu = 1/2$ [15], a composite fermion state at $\nu = 2/3$ [16], and a Moore-Read Pfaffian state [17] at $\nu = 1$ [18]. Coupling of two Bose gases in *parallel* magnetic fields leads to a richer variety of phases as studied in both regimes of vortex lattices [19, 20] and QH states [21–26]. We will make comparisons between the cases of parallel and antiparallel magnetic fields in the course of our analyses.

Our main results for pseudospin-$\frac{1}{2}$ Bose gases in *antiparallel* magnetic fields are summarized in Fig. 1. For large $\nu_{\rm tot}$ ($\gg 1$), we show that within the Gross-Pitaevskii (GP) mean field theory, the present system shows exactly the same vortex lattices as the case of parallel magnetic fields studied previously [19, 20]. For small $\nu_{\rm tot}$, we find through exact diagonalization calculations that (fractional) QSH states, which are well approximated by two independent QH states, are remarkably robust and survive even when $g_{\uparrow\downarrow} \approx g$. While similar bosonic systems have also been studied previously [11, 27], our calculations provide a more systematic determination of the ranges of these QSH states. For $g_{\uparrow\downarrow} = -g$, we obtain exact many-body GSs with a novel paring nature.

Here we comment on the connections with related studies. A similar problem of two coupled fractional QH states with opposite chiralities have been studied in models of interacting spin-$\frac{1}{2}$ fermions in lattices [28] and in continuous space [29], and in a model of strained graphene [30]. Compared to lattice systems [28, 30], our simple setting can provide a clearer picture of the interplay between intracomponent and intercomponent interactions. Reference [29] focused on $\nu_{\rm tot} = 2/3$, where two fermionic Laughlin states are coupled; our phase diagram for $\nu_{\rm tot} = 1$ (corresponding to two coupled bosonic Laughlin states) have some similarities with the result of Ref. [29]. Strong coupling of two QH systems can potentially lead to novel TR-invariant topological states (beyond simple product states) as proposed in Refs. [8, 31–34]. However, none of such phases were found in our extensive numerical search in the present model (see the Supplemental Material [12]), leaving open the issue of finding physical settings for realizing such states. The stability of gapless edge states in coupled QH systems in the presence of intercomponent tunneling has also been discussed [28, 35–37]. Although this is an interesting issue, we focus on bulk properties in the absence of such tunneling and do not address edge properties in this Letter.

We consider a system of a two-dimensional (2D) pseudospin-$\frac{1}{2}$ Bose gas (in the xy plane) subject to antiparallel magnetic fields $\pm B$ along the z axis for spin states $\alpha =\uparrow$ and $\downarrow$. We introduce the fictitious charge q of a particle, and assume $qB > 0$. We denote the strengths of the intracomponent and intercomponent contact interactions by g and $g_{\uparrow\downarrow}$, respectively. In the second-quantized form, the interaction Hamiltonian is written as

$$H_{\rm int} = \sum_{\alpha,\beta=\uparrow,\downarrow} \frac{g_{\alpha\beta}}{2} \int d^2\boldsymbol{r} \hat{\Psi}^\dagger_\alpha(\boldsymbol{r}) \hat{\Psi}^\dagger_\beta(\boldsymbol{r}) \hat{\Psi}_\beta(\boldsymbol{r}) \hat{\Psi}_\alpha(\boldsymbol{r}), \quad (1)$$

where $\hat{\Psi}_\alpha(\boldsymbol{r})$ is a bosonic field operator for the spin state α. We set $g_{\uparrow\uparrow} = g_{\downarrow\downarrow} \equiv g > 0$ and $g_{\uparrow\downarrow} = g_{\downarrow\uparrow}$.

Let us first consider the regime of large $\nu_{\rm tot} (\gg 1)$, where the system is expected to be well described by the GP mean field theory. In the GP theory, the condensate wave functions, $\Psi_\uparrow(\boldsymbol{r})$ and $\Psi_\downarrow(\boldsymbol{r})$, are determined by minimizing the GP energy functional

$$E[\Psi_\uparrow, \Psi_\downarrow] = \int d^2\boldsymbol{r} \Big[\Psi^*_\uparrow \mathcal{K}(B) \Psi_\uparrow + \Psi^*_\downarrow \mathcal{K}(-B) \Psi_\downarrow + \sum_{\alpha,\beta} \frac{g_{\alpha\beta}}{2} |\Psi_\alpha|^2 |\Psi_\beta|^2 \Big] \quad (2)$$

with $\mathcal{K}(B) = \frac{1}{2M}[(-i\hbar\partial_x + qBy)^2 + (-i\hbar\partial_y)^2]$. Noting $\int d^2\boldsymbol{r} \Psi^*_\downarrow \mathcal{K}(-B) \Psi_\downarrow = \int d^2\boldsymbol{r} \Psi_\downarrow \mathcal{K}(B) \Psi^*_\downarrow$, we find that the present system reduces to the case of parallel magnetic fields by the replacement $\Psi_\downarrow \to \Psi^*_\downarrow$, for which case the mean-field phase diagram is known [19, 20] and summarized as follows. When $g_{\uparrow\downarrow} = 0$, each component independently forms a triangular vortex lattice. The two triangular lattices overlap for $g_{\uparrow\downarrow} < 0$ and are displaced from each other for small $g_{\uparrow\downarrow}/g > 0$. When increasing the coupling ratio in the range $0 < g_{\uparrow\downarrow}/g < 1$, the interlocked two lattices undergo phase transitions from triangular to square (by taking a complex conjugate for the $\downarrow$ component in these states, we obtain insets of Fig. 1). For $g_{\uparrow\downarrow}/g > 1$, the system displays exotic metastable states, such as double-core lattices, stripes, and vortex sheets.

Next we consider the regime of $\nu_{\rm tot} = O(1)$, where the system is expected to be strongly correlated. We assume that B is so large that the interaction energy is much smaller than the Landau-level spacing $\hbar qB/M$. In this case, restriction to the lowest Landau level (LLL) is legitimate. Within this restricted subspace, we have performed an exact diagonalization analysis of the interaction Hamiltonian (1). Here, we have employed a sphere geometry [38] (see also the Supplemental Material [12]), which has no edge and is useful for studying bulk properties around the center of a trapped gas. We place magnetic monopoles of charges $\pm N_\phi(2\pi\hbar/q)$ with integer $N_\phi \equiv 2S$ at the center of the sphere; these monopoles produce magnetic fields $\pm B$ for the $\uparrow$ and $\downarrow$ components, respectively, on the sphere of radius $R = \ell\sqrt{S}$, where $\ell = \sqrt{\hbar/(qB)}$ is the magnetic length. Introducing the spherical coordinates (θ, φ), single-particle orbits in the LLL are given by $\psi_{m\downarrow} \propto u^{S+m} v^{S-m}$ with $u = \cos(\theta/2) e^{i\varphi/2}$ and $v = \sin(\theta/2) e^{-i\varphi/2}$ for the $\downarrow$ component and $\psi_{m\uparrow} = (-1)^{S-m} \psi^*_{-m,\downarrow}$ for the $\uparrow$ component,

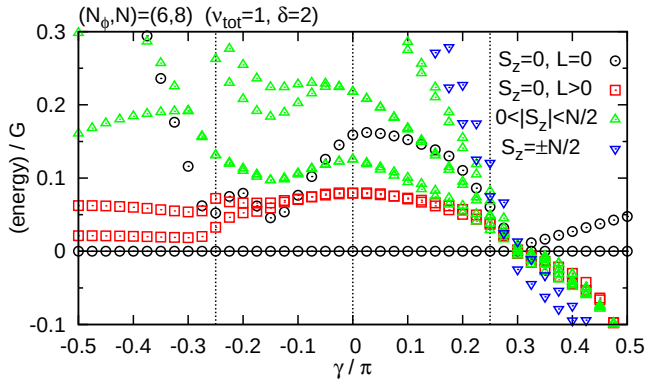

FIG. 2: (color online) Energy spectra versus $\gamma/\pi = \arctan(g_{\uparrow\downarrow}/g)/\pi$ for $(N_\phi, N) = (6, 8)$. The eigenstates are classified by $S_z = (N_\uparrow - N_\downarrow)/2$ and the total angular momentum L. The two lowest eigenenergies in each sector are displayed. The lowest eigenenergy in the sector $(S_z, L) = (0, 0)$ is subtracted from the entire spectrum. Vertical dotted lines correspond to $g_{\uparrow\downarrow}/g = 0, \pm 1$.

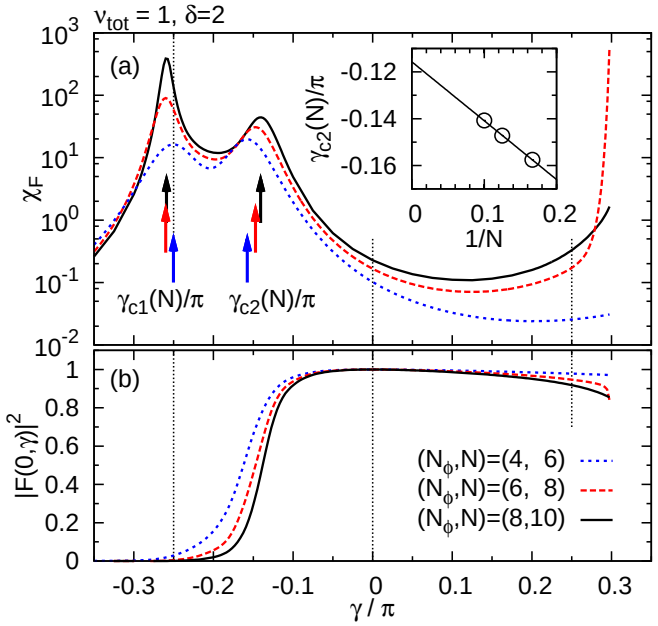

FIG. 3: (color online) (a) Fidelity susceptibility $\chi_F(\gamma)$ as a function of γ/π. Three system sizes (N_ϕ, N) with the filling factor $\nu_{\rm tot} = 2$ and the shift $\delta = 2$ are chosen to discuss the stability of a fractional QSH state composed of two Laughlin states. Peak positions indicated by arrows give finite-size estimates of the transition points. The inset shows an extrapolation of $\gamma_{c2}(N)/\pi$ to the thermodynamic limit using a linear function of $1/N$. (b) Squared overlap with the decoupled case, i.e., $|F(0,\gamma)|^2$. Vertical dotted lines correspond to $\gamma = 0, \pm\pi/4$.

where $m = -S, -S+1, \ldots, S$ is the z-component of the angular momentum. The many-body eigenstates can be classified by the total angular momentum L. For incompressible states on finite spheres, the relation between N and N_ϕ involves a characteristic shift δ: $N = \nu_{\rm tot}(N_\phi + \delta)$, where δ depends on an individual candidate wave function. Incompressible GSs appear in general in the sector with $L = 0$ for (N_ϕ, N) satisfying this relation. The QSH states at $\nu = 1, 4/3, 2$ in Fig. 1 have $\delta = 2, 3, 2$, respectively.

We present our numerical results for $\nu_{\rm tot} = 1$ and $\delta = 2$, where the stability of the QSH states composed of two Laughlin states can be analyzed. The two components are expected to become entangled as the magnitude of $g_{\uparrow\downarrow}/g$ increases. We set $g = G\ell^2 \cos\gamma$ and $g_{\uparrow\downarrow} = G\ell^2 \sin\gamma$ with $G > 0$, and change γ in the range $-\pi/2 \le \gamma \le \pi/2$. Figure 2 displays energy spectra as a function of γ/π for $(N_\phi, N) = (6, 8)$. While we are interested in the population-balanced case $N_\uparrow = N_\downarrow$, we perform calculations for the imbalanced case $N_\uparrow \neq N_\downarrow$ as well to discuss a potential instability towards a phase separation. The eigenstates are classified by $S_z = (N_\uparrow - N_\downarrow)/2$ and L. At $\gamma = 0$, a finite energy gap $\Delta/G \approx 0.08$ appears above the unique GS; this gap value coincides with that calculated for a scalar gas with 4 particles [16]. The GS stays in the sector $(S_z, L_{\rm tot}) = (0, 0)$ for $\gamma/\pi \lesssim 0.3$. For $\gamma/\pi \gtrsim 0.3$, the GS is replaced by a maximally imbalanced state with $S_z = \pm N/2$. This indicates that even for balanced populations $N_1 = N_2$, the system locally favors formation of a single-component domain, leading to a phase separation. Around $\gamma/\pi \approx -0.25$ and -0.15, some energy levels show extrema. In fact, phase transitions occur around these points, as we discuss next.

To detect phase transitions, we have calculated the fidelity susceptibility χ_F [39] as a function of γ; see Fig. 3(a). When two parameter points γ and $\gamma + \delta\gamma$ are close enough, the overlap between the GSs at these points can be expanded as $F(\gamma, \gamma+\delta\gamma) \equiv |\langle\Psi(\gamma)|\Psi(\gamma+\delta\gamma)\rangle| = 1 - \frac{\chi_F}{2}(\delta\gamma)^2 + \ldots$, which allows us to define the fidelity susceptibility $\chi_F(\gamma) = -2\lim_{\delta\gamma\to 0}[\ln F(\gamma, \gamma+\delta\gamma)]/(\delta\gamma)^2$. For $\gamma < 0$, we observe two peaks in $\chi_F(\gamma)$, which indicate phase transitions; these peaks shift gradually and grow sharper with increasing N. The peak positions, $\gamma_{c1}(N)/\pi$ and $\gamma_{c2}(N)/\pi$ [arrows in Fig. 3(a)], can be used to make a finite-size estimation of the transition points. The extrapolation of $\gamma_{c2}(N)$ to the thermodynamic limit gives $\gamma_{c2} \approx -0.12\pi$ [inset of Fig. 3(a)]. The data of $\gamma_{c1}(N)$, by contrast, are located around $-\pi/4$ and do not depend smoothly on N; yet, we later discuss that $\gamma_{c1} = -\pi/4$ gives the exact transition point in the thermodynamic limit. For $\gamma > 0$, no peak appears in $\chi_F(\gamma)$ until the GS level crossing occurs as in Fig. 2. This indicates that a single phase is formed over $-0.12 \lesssim \gamma/\pi \lesssim 0.30$ (i.e., $-0.38 \lesssim g_{\uparrow\downarrow}/g \lesssim 1.4$). Figure 3(b) shows the squared overlap with the GS at $\gamma = 0$: $|F(0,\gamma)|^2$. We find that $|F(0,\gamma)|^2$ indeed stays close to unity in the above range, indicating that a fractional QSH state, which is well ap-

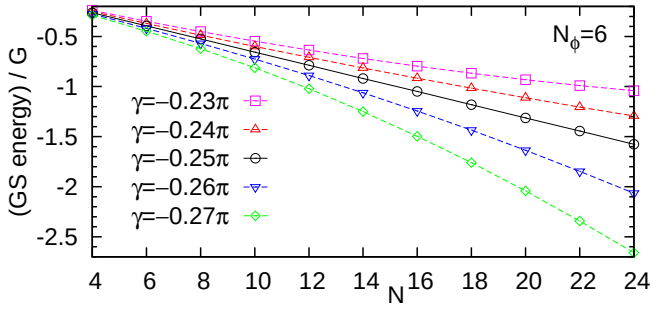

FIG. 4: (color online) Ground-state energy as a function of N with $N_\phi = 6$ for different values of γ around the exact transition point $-\pi/4$.

proximated by the product of two independent Laughlin states, is realized over this range. This range is remarkably wide as it includes the case of $g_{\uparrow\downarrow} \approx g$. The nature of the phase for $-0.25 < \gamma/\pi \lesssim -0.12$ is currently unclear from the numerical data; yet the global phase structure in Fig. 1 suggests that overlapping triangular vortex lattices at high $\nu_{\rm tot}$ persist down to this low-$\nu_{\rm tot}$ regime. We have performed similar analyses for $\nu_{\rm tot} = 4/3$ and 2 and found that QSH states continue to be the GSs over wide regions; see Fig. 1 and the Supplemental Material [12]. This sharply contrasts with the case of parallel magnetic fields, where the product of two QH states persists only up to $g_{\uparrow\downarrow}/g \approx 0.6$ [22] and 0.2 [26] for $\nu_{\rm tot} = 4/3$ and 2, respectively.

Finally, we discuss the case of $g_{\uparrow\downarrow} = -g$, where the exact many-body GSs can be derived within the LLL manifold. Using the LLL states on a sphere, the field operator can be expanded as $\hat{\Psi}_\alpha(\boldsymbol{r}) = \sum_m b_{m\alpha}\psi_{m\alpha}(\boldsymbol{r})$, from which one can derive the equal-position commutation relation $[\hat{\Psi}_\alpha(\boldsymbol{r}), \hat{\Psi}^\dagger_\beta(\boldsymbol{r})] = \delta_{\alpha\beta}(2S+1)/(4\pi S\ell^2)$. Using this, the interaction Hamiltonian (1) can be rewritten as

$$H_{\rm int} = \frac{g}{2}\int d^2\boldsymbol{r}\,[\rho_\uparrow(\boldsymbol{r}) - \rho_\downarrow(\boldsymbol{r})]^2 - \frac{g}{\ell^2}\frac{2S+1}{8\pi S}(N_\uparrow + N_\downarrow), \tag{3}$$

where $\rho_\alpha(\boldsymbol{r}) = \hat{\Psi}^\dagger_\alpha(\boldsymbol{r})\hat{\Psi}_\alpha(\boldsymbol{r})$ is the density operator. Thus the GS can be obtained by minimizing the squared density difference $[\rho_\uparrow(\boldsymbol{r}) - \rho_\downarrow(\boldsymbol{r})]^2$ as much as possible for every point $\boldsymbol{r}$ in the space. In fact, one can make this difference vanish everywhere. To see it, we introduce the operator $K_+ = \int d\boldsymbol{r}\hat{\Psi}^\dagger_\uparrow(\boldsymbol{r})\hat{\Psi}^\dagger_\downarrow(\boldsymbol{r})$, which creates a tightly bound pair of $\uparrow$ and $\downarrow$ particles uniformly in space. One can show that K_+ commutes with the density difference $\rho_\uparrow(\boldsymbol{r}) - \rho_\downarrow(\boldsymbol{r})$. Therefore, starting from the vacuum $|0\rangle$ and repeatedly operating K_+ on it, we can make the density difference vanish everywhere. The GS for particle numbers $N_\uparrow = N_\downarrow = N/2$ is thus obtained as $|\Psi\rangle(N) \propto K_+^{N/2}|0\rangle$, whose energy is given by the last term in Eq. (3): $E_{\rm GS}(N) = -\frac{g}{\ell^2}\frac{2S+1}{8\pi S}N$. The linear dependence on N obtained here is quite unusual; it indicates that the compressibility $\kappa = \left[\frac{N^2}{4\pi R^2}\frac{d^2E_{\rm GS}}{dN^2}\right]^{-1}$ diverges. Some other exact results such as a hidden su(1,1) structure, the paring amplitude, and excited states are presented in the Supplemental Material [12].

We note that at the point $g_{\uparrow\downarrow}/g = -1$ (i.e., $\gamma = -\pi/4$), κ changes the sign. Figure 4 displays the numerically calculated GS energy as a function of N with $N_\phi = 6$. We find that the dependence on N is convex for $\gamma > -\pi/4$ and concave for $\gamma < -\pi/4$, indicating positive and negative κ, respectively. The states with $\kappa < 0$ are thermodynamically unstable and spontaneously shrink, leading to a collapse of the gas.

In summary, we have obtained the global phase diagram of two-component Bose gases in antiparallel magnetic fields as presented in Fig. 1. We have found that QSH states composed of two nearly independent QH states are remarkably stable and persists even for $g_{\uparrow\downarrow} \approx g$. This sharply contrasts with the case of parallel magnetic fields, where SU(2)-symmetric QH states (with high entanglement between the two components) emerge for $g_{\uparrow\downarrow} = g$ at $\nu_{\rm tot} = 4/3$ [21, 22, 25] and 2 [23–26]. In spite of this marked difference between the cases of parallel and antiparallel magnetic fields at low $\nu_{\rm tot}$, we have shown within the GP mean field theory that at high $\nu_{\rm tot}(\gg 1)$, the two cases show the same vortex phase diagrams. It is expected that the present study can serve as a useful reference point for studying the interplay between strong correlations and TR symmetry in a wider variety of settings.

The authors thank M. A. Cazalilla and Y. Horinouchi for useful discussions. This work was supported by KAKENHI Grant Nos. 25800225 and 22340114 from the Japan Society for the Promotion of Science, and by a Grant-in-Aid for Scientific Research on Innovation Areas "Topological Quantum Phenomena" (KAKENHI Grant No. 22103005) and the Photon Frontier Network Program from MEXT of Japan.

Note added. After completion of this work, we became aware of an independent work by Repellin *et al.* [40], where the stability of two coupled bosonic Laughlin states is investigated in lattice models. Although their models were different from ours, they also reach a conclusion that the product of two Laughlin states with opposite chiralities persists over a wider range of the intercomponent coupling than the case of the same chiralities.

[1] J. Dalibard, F. Gerbier, G. Juzeliūnas, and P. Öhberg, Rev. Mod. Phys. **83**, 1523 (2011).
[2] N. Goldman, G. Juzeliūnas, P. Öhberg, I. B. Spielman, arXiv:1308.6533.
[3] Y.-J. Lin, R. L. Compton, K. Jinménez-García, J. V. Porto, and I. B. Spielman, Nature **462**, 628 (2009).
[4] M. C. Beeler, R. A. Williams, K. Jiménez-Garcia, L. J.

LeBlanc, A. R. Perry, and I. B. Spielman, Nature **498**, 201 (2013).
[5] M. Aidelsburger, M. Atala, M. Lohse, J. T. Barreiro, B. Paredes, and I. Bloch, Phys. Rev. Lett. **111**, 185301 (2013);
[6] C. J. Kennedy, G. A. Siviloglou, H. Miyake, W. C. Burton, W. Ketterle, Phys. Rev. Lett. **111**, 225301 (2013).
[7] C. L. Kane and E J. Mele, Phys. Rev. Lett. **95**, 226801 (2005); Phys. Rev. Lett. **95**, 146802 (2005).
[8] B. A. Bernevig, and S.-C. Zhang, Phys. Rev. Lett. **96**, 106802 (2006).
[9] M. König, S. Wiedmann, C. Brüne, A. Roth, H. Buhmann, L. W. Molenkamp, X.-L. Qi, and S.-C. Zhang, Science **318**, 766 (2007).
[10] B. A. Bernevig, T. L. Hughes, and S.-C. Zhang, Science **314**, 1757 (2006).
[11] X.-J. Liu, X. Liu, L. C. Kwek, and C. H. Oh, Phys. Rev. B **79**, 165301 (2009).
[12] See the Supplemental Material for the representation of the Hamiltonian in the LLL basis on a sphere, further numerical results (in particular, those for $\nu_{\rm tot} = \frac{4}{3}$ and 2), and more details on the exact results at the point $g_{\uparrow\downarrow} = -g$.
[13] For a review, see N. R. Cooper, Adv. Phys. **57**, 539 (2008).
[14] J. R. Abo-Shaeer, C. Raman, J. M. Vogels, and W. Ketterle, Science **292**, 476 (2001).
[15] N. K. Wilkin, J. M. F. Gunn, and R. A. Smith, Phys. Rev. Lett. **80**, 2265 (1998).
[16] N. Regnault and Th. Jolicoeur, Phys. Rev. Lett. **91**, 030402 (2003); Phys. Rev. B **69**, 235309 (2004).
[17] G. Moore and N. Read, Nucl. Phys. **B360**, 362 (1991).
[18] N. R. Cooper, N. K. Wilkin, and J. M. F. Gunn, Phys. Rev. Lett. **87**, 120405 (2001).
[19] E. J. Mueller and T.-L. Ho, Phys. Rev. Lett. **88**, 180403 (2002).
[20] K. Kasamatsu, M. Tsubota, and M. Ueda, Phys. Rev. Lett. **91**, 150406 (2003); Int. J. Mod. Phys. B **19**, 1835 (2005).
[21] T. Graß, B. Juliá-Díaz, N. Barberán, and M. Lewenstein, Phys. Rev. A **86**, 021603 (R) (2012).
[22] S. Furukawa and M. Ueda, Phys. Rev. A **86**, 031604 (R) (2012).
[23] T. Senthil and M. Levin, Phys. Rev. Lett. **110**, 046801 (2013).
[24] S. Furukawa and M. Ueda, Phys. Rev. Lett. **111**, 090401 (2013).
[25] Y.-H. Wu and J. K. Jain, Phys. Rev. B **87**, 245123 (2013).
[26] N. Regnault and T. Senthil, Phys. Rev. B **88**, 161106 (2013).
[27] O. Fialko, J. Brand, and U. Zülicke, New J. Phys. **16**, 025006 (2014).
[28] T. Neupert, L. Santos, S. Ryu, C. Chamon, and C. Mudry, Phys. Rev. B **84**, 165107 (2011).
[29] H. Chen and K. Yang, Phys. Rev. B **85**, 195113 (2012).
[30] P. Ghaemi, J. Cayssol, D. N. Sheng, and A. Vishwanath, Phys. Rev. Lett. **108**, 266801 (2012).
[31] L. Santos, T. Neupert, S. Ryu, C. Chamon, and C. Mudry, Phys. Rev. B **84**, 165138 (2011).
[32] M. Levin and A. Stern, Phys. Rev. B **86**, 115131 (2012).
[33] Y.-M. Lu and A. Vishwanath, Phys. Rev. B **86**, 125119 (2012).
[34] X. Chen, Z.-C. Gu, Z.-X. Liu, and X.-G. Wen, Science **338**, 1604 (2012); Phys. Rev. B **87**, 155114 (2013).
[35] M. Levin and A. Stern, Phys. Rev. Lett. **103**, 196803 (2009).
[36] A. Cappelli and E. Randellini, Journal of High Energy Physics, **12**, 101 (2013).
[37] M. Koch-Janusz and Z. Ringel, arXiv:1311.6507.
[38] F. D. M. Haldane, Phys. Rev. Lett. **51**, 605 (1983)
[39] W.-L. You, Y.-W. Li, and S.-J. Gu, Phys. Rev. E **76**, 022101 (2007).
[40] C. Repellin, B. A. Bernevig, and N. Regnault, arXiv:1402.2652.

Supplemental Material

Hamiltonian in the lowest-Landau-level basis on a sphere

Here we describe some basic knowledge on the lowest-Landau-level (LLL) basis on a sphere [1, 2] in our time-reversal-invariant setting, and derive the representation of the interaction Hamiltonian in this basis. We also briefly explain the numerical methods that we used for diagonalizing this Hamiltonian.

We introduce the polar coordinates (r, θ, ϕ) and the associated unit vectors $\boldsymbol{e}_r$, $\boldsymbol{e}_\theta$, $\boldsymbol{e}_\phi$. We place magnetic monopoles of charges $\pm N_\phi(2\pi\hbar/q)$ with integer $N_\phi \equiv 2S$ at the center of the sphere; these monopoles produce magnetic fields $\pm B\boldsymbol{e}_r$ for the $\uparrow$ and $\downarrow$ components, respectively, on the sphere of radius $R = \ell\sqrt{S}$, where $\ell = \sqrt{\hbar/|qB|}$ is the magnetic length. We assume $qB > 0$ in the following. The single-particle Hamiltonian h_α for the spin state $\alpha(=\uparrow,\downarrow)$ on the sphere is given by

$$h_\alpha = \frac{1}{2M}\left[\boldsymbol{e}_r \times (\boldsymbol{p} - q\boldsymbol{A}_\alpha)\right]^2 = \frac{\boldsymbol{\Lambda}_\alpha^2}{2MR^2}, \tag{4}$$

with

$$\boldsymbol{A}_{\uparrow,\downarrow} = \mp N_\phi \frac{2\pi\hbar}{q}\frac{\cot\theta}{4\pi r}\boldsymbol{e}_\phi, \tag{5}$$

$$\boldsymbol{\Lambda}_\alpha = \boldsymbol{r} \times (\boldsymbol{p} - q\boldsymbol{A}_\alpha). \tag{6}$$

One can show that $\boldsymbol{L}_{\uparrow,\downarrow} = \boldsymbol{\Lambda}_{\uparrow,\downarrow} \mp \hbar S\boldsymbol{e}_r$ obey the standard algebra of angular momenta; henceforth we simply call $\boldsymbol{L}_{\uparrow,\downarrow}$ angular momenta. Noticing $\boldsymbol{\Lambda}_\alpha^2 = \boldsymbol{L}_\alpha^2 - \hbar^2 S^2$, one finds that the eigenvalues of $\boldsymbol{\Lambda}_\alpha^2$ are given by $\hbar^2[l(l+1) - S^2]$, where l is the magnitude of the angular momentum $\boldsymbol{L}_\alpha$. Because $\boldsymbol{\Lambda}_\alpha^2 \geq 0$, the minimum of l is given by $l = S$.

The LLL on a sphere is thus given by the states with the angular momentum $l = S$. Their wave functions are given by

$$\psi_{m\uparrow}(\boldsymbol{r}) = \frac{1}{R}\left[\frac{2S+1}{4\pi}C(2S, S-m)\right]^{\frac{1}{2}}(v^*)^{S+m}(-u^*)^{S-m} \tag{7a}$$

$$\psi_{m\downarrow}(\boldsymbol{r}) = \frac{1}{R}\left[\frac{2S+1}{4\pi}C(2S, S+m)\right]^{\frac{1}{2}}u^{S+m}v^{S-m}, \tag{7b}$$

where $m = -S, -S+1, \ldots, S$ is the z-component of the angular momentum, $C(\cdot,\cdot)$ is the binomial coefficient, and

$$u = \cos\left(\frac{\theta}{2}\right) e^{i\phi/2}, \quad v = \sin\left(\frac{\theta}{2}\right) e^{-i\phi/2}. \tag{8}$$

These wave functions satisfy the relations

$$\psi_{m\uparrow} = (-1)^{S-m}\psi^*_{-m,\downarrow}, \quad \psi_{m\downarrow} = (-1)^{S+m}\psi^*_{-m,\uparrow}. \tag{9}$$

We now consider the interaction Hamiltonian

$$H_{\rm int} = \sum_{\alpha,\beta=\uparrow,\downarrow} \frac{g_{\alpha\beta}}{2} \int d^2\boldsymbol{r} \hat{\Psi}^\dagger_\alpha(\boldsymbol{r})\hat{\Psi}^\dagger_\beta(\boldsymbol{r})\hat{\Psi}_\beta(\boldsymbol{r})\hat{\Psi}_\alpha(\boldsymbol{r}) \tag{10}$$

with $g_{\uparrow\uparrow} = g_{\downarrow\downarrow} = g > 0$ and $g_{\uparrow\downarrow} = g_{\downarrow\uparrow}$. In the LLL approximation, the field operators are expanded as

$$\hat{\Psi}_\alpha(\boldsymbol{r}) = \sum_{m=-S}^{S} b_{m\alpha}\psi_{m\alpha}(\boldsymbol{r}). \tag{11}$$

Substituting these into Eq. (10), we obtain

$$H_{\rm int} = \sum_{\alpha,\beta} \sum_{m_1,m_2,m_3,m_4} V^{\alpha\beta}_{m_1m_2m_3m_4} b^\dagger_{m_1\alpha} b^\dagger_{m_2\beta} b_{m_3\beta} b_{m_4\alpha}, \tag{12}$$

where

$$V^{\alpha\beta}_{m_1m_2m_3m_4} = \frac{g_{\alpha\beta}}{2} \int d^2\boldsymbol{r} \psi^*_{m_1\alpha}(\boldsymbol{r})\psi^*_{m_2\beta}(\boldsymbol{r})\psi_{m_3\beta}(\boldsymbol{r})\psi_{m_4\alpha}(\boldsymbol{r}). \tag{13}$$

Using Eq. (7), the coefficients (13) are calculated as

$$V^{\alpha\alpha}_{m_1m_2m_3m_4} = \delta_{m_1+m_2,m_3+m_4} \frac{g}{8\pi\ell^2} \times \frac{(2S+1)^2}{S(4S+1)} \frac{\left(\prod_i C(2S,S+m_i)\right)^{1/2}}{C(4S,2S+m_1+m_2)}, \tag{14}$$

$$V^{\uparrow\downarrow}_{m_1m_2m_3m_4} = \delta_{m_1+m_2,m_3+m_4}(-1)^{2S-m_1-m_4} \frac{g_{\uparrow\downarrow}}{8\pi\ell^2} \times \frac{(2S+1)^2}{S(4S+1)} \frac{\left(\prod_i C(2S,S+m_i)\right)^{1/2}}{C(4S,2S+m_1-m_3)}. \tag{15}$$

The total angular momentum $\boldsymbol{L}^{\rm tot}$ can be expressed in the second-quantized form as

$$L^{\rm tot}_+ = L^{\rm tot}_x + iL^{\rm tot}_y = \sum_{m,\alpha} \sqrt{(S-m)(S+m+1)}\, b^\dagger_{m+1\alpha} b_{m\alpha},$$
$$L^{\rm tot}_- = L^{\rm tot}_x - iL^{\rm tot}_y = (L^{\rm tot}_+)^\dagger, \quad L^{\rm tot}_z = \sum_{m,\alpha} m b^\dagger_{m\alpha} b_{m\alpha}. \tag{16}$$

These commute with the Hamiltonian (12). Therefore, the eigenstates of Eq. (12) can be classified by the magnitude L and the z-component eigenvalue L_z of $\boldsymbol{L}^{\rm tot}$.

We performed exact diagonalization calculations of the Hamiltonian (12). Restriction to the subspace of fixed particle numbers (N_1, N_2) and z-component total angular momentum L_z can easily be implemented by an appropriate choice of the Fock basis $\{|\{n_{m\alpha}\}\rangle\}$, where n_m is the eigenvalue of $b^\dagger_{m\alpha}b_{m\alpha}$. Restriction to specific $L = L_{\rm target}$ can be done by first choosing the sector with $L_z = L_{\rm target}$ and adding to the Hamiltonian the term $\lambda L^{\rm tot}_- L^{\rm tot}_+$, where λ is a positive constant. This term shifts the entire eigenspectrum by $\lambda[L(L+1) - L_z(L_z+1)]$. The states with $L > L_{\rm target}$ can therefore be eliminated from the low-energy subspace of our interest by taking sufficiently large $\lambda > 0$. We used a LAPACK full diagonalization routine, an ARPACK routine [3] of the implicitly restarted Lanczos method, and the standard Lanczos method (storing only a minimum of two Lanczos vectors at each iteration) for small, medium, and large system sizes. The second method requires a larger memory space for Lanczos vectors than the third, but is more stable against the presence of eigenenergy degeneracies. In fact, the present time-reversal-invariant Hamiltonian often involves such degeneracies, and the standard Lanczos method sometimes (but not always) did not converge properly (for all presented data calculated by this method, we have checked sufficient convergence). The addition of the term for the L-restriction mentioned above makes the convergence even worse (because the matrix to be diagonalized becomes less sparse); we therefore imposed this restriction only with LAPACK and ARPACK routines. Even when we did not do so, we could determine the L value of each eigenstate by operating $(\boldsymbol{L}^{\rm tot})^2$ on it. In Fig. 5, for example, we used the standard Lanczos method without the L-restriction for large system sizes, but could still determine the L value of the ground state in this way.

Numerical search for incompressible states

Through exact diagonalization calculations on a sphere geometry, we carried out an extensive search for incompressible ground states (GS) in the (N_ϕ, N) plane for different values of $\gamma = \arctan(g_{\uparrow\downarrow}/g)$; see Fig. 5. Incompressible states in general appear as unique GSs with $L = 0$, which are indicated by filled circles in Fig. 5. The area of each filled circle is proportional to the neutral gap Δ_n, which is defined as the excitation gap for fixed $(N_\phi, N_\uparrow, N_\downarrow)$. It is known that for incompressible states on a finite sphere, the relation between N and N_ϕ involves a characteristic shift δ; $N = \nu_{\rm tot}(N_\phi + \delta)$, where δ depends on an individual candidate wave function. Solid lines indicate this relation for $(\nu_{\rm tot}, \delta) = (k, 2)$ with $k = 1, 2, 3, 4$; these correspond to the quantum spin Hall (QSH) states made of two Read-Rezayi states [4] and include in particular the cases of two Laughlin ($k = 1$) or Moore-Read ($k = 2$) states (we note that these states appear only for even N_ϕ). Broken lines indicate the N-N_ϕ relation for $(\nu_{\rm tot}, \delta) = (\frac{2p}{p+1}, p+1)$ with $p = 2, 3$; these

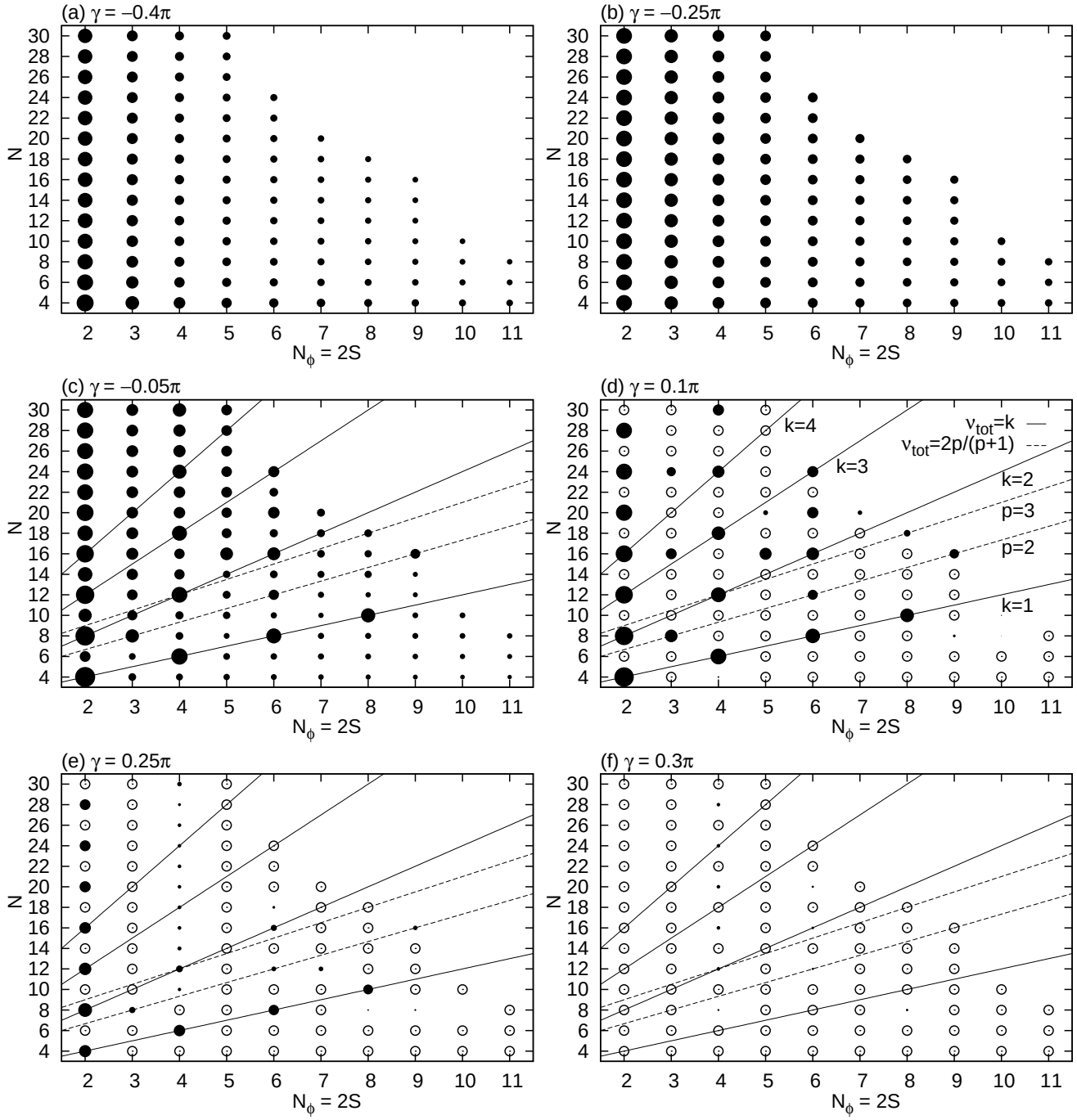

FIG. 5: Candidates for incompressible GSs in the (N_ϕ, N) plane, calculated on a sphere geometry for different values of $\gamma = \arctan(g_{\uparrow\downarrow}/g)$. Filled circles indicate GSs with the total angular momentum $L = 0$, where incompressible states can appear; the area of each filled circle is proportional to the neutral gap Δ_n. Empty circles indicate the GSs with $L > 0$. Solid and broken lines indicate the relations $N = \nu(N_\phi + \delta)$ for $(\nu_{\rm tot}, \delta) = (k, 2)$ and $(\frac{2p}{p+1}, p+1)$, respectively. The QSH states composed of a pair of Laughlin, composite fermion, and Moore-Read states appear for $(\nu_{\rm tot}, \delta) = (1, 2)$, $(\frac{4}{3}, 3)$, and $(2, 2)$, respectively. Data points are missing for large N_ϕ or N due to an exponentially increasing computation time.

correspond to the QSH states made of two composite fermion states in Jain's principal sequence.

We first analyze the cases of $\gamma > 0$. For (d) $\gamma = 0.1\pi$ and (e) $\gamma = 0.25\pi$, we find that the $L = 0$ GSs appear for (N_ϕ, N) on the solid and broken lines. However, the values of the neutral gap are much smaller in (e). For (f) $\gamma = 0.3\pi$, most of the $L = 0$ GSs disappear; even when they survive, the gap values are very small. Comparing (e) with (d), we do not find the emergence of any new $L = 0$ GS with an appreciable energy gap above it. This indicates that within the present model, increasing $g_{\uparrow\downarrow}/g$ only gradually diminishes the energy gaps of QSH states made of two quantum Hall (QH) states and does not produce any new incompressible state. A possible emergence of a new incompressible state in the presence of other perturbations such as the introduction of an optical lattice or longer-range interactions is an interesting future problem.

We next analyze the cases of $\gamma < 0$. In this case, $L = 0$ GSs appear for all (N_ϕ, N) we have investigated. However, it is important to analyze whether the energy gaps above these GSs remain in the thermodynamic limit. For (c) $\gamma = -0.05\pi$, the energy gaps are comparatively large on the solid and broken lines, and finite energy gaps possibly remain on these lines in the thermodynamic limit. The energy gaps for other (N_ϕ, N) tend to decrease as we increase N_ϕ. Remarkably, for (b) $\gamma = -0.25\pi$, the energy gaps do not depend on N at all, and decrease monotonically as a function of N_ϕ. At this point, an exact expression for the excitation energy can be found as we explain later; see Eq. (34). Since the energy gap vanishes as $N_\phi \to \infty$, no incompressible state appears. The energy gaps for (a) $\gamma = -0.4\pi$ also shows a tendency to vanish as $N_\phi \to \infty$. At this parameter point, the system is not stable and spontaneously collapse as explained in the main text.

This section has focused on a global picture of the types and the ranges of incompressible states present in the model. More precise determination of the ranges of the QSH phases requires more detailed analyses, which are done for $\nu_{\rm tot} = 1$ in the main text and for $\nu_{\rm tot} = \frac{4}{3}$ and 2 in the next section.

Numerical analyses for $\nu_{\rm tot} = \frac{4}{3}$ and 2

Here we explain our numerical analyses for $\nu_{\rm tot} = 4/3$ and 2. For $g_{\uparrow\downarrow} = 0$, the GSs at these $\nu_{\rm tot}$ are given by QSH states composed of two independent composite fermion or Moore-Read states, which have $\delta = 3$ and 2, respectively. We discuss the stability of such QSH states in the presence of the intercomponent coupling $g_{\uparrow\downarrow}$. We perform essentially the same lines of analysis as the $\nu_{\rm tot} = 1$ case discussed in the main text.

Figure 6 displays the energy spectra as a function of $\gamma/\pi = \arctan(g_{\uparrow\downarrow}/g)/\pi$. Increasing γ/π from zero,

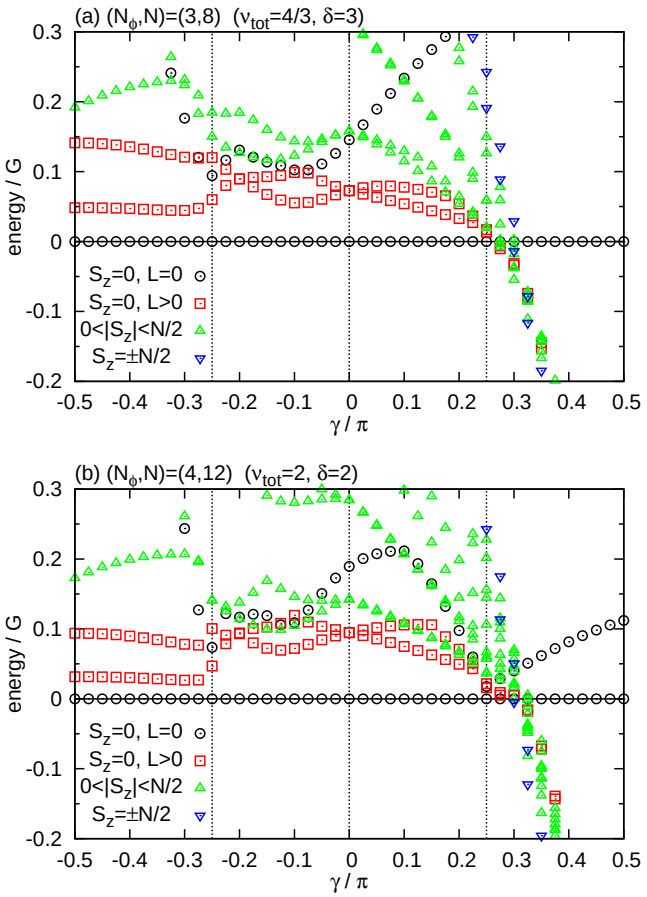

FIG. 6: Energy spectra versus $\gamma/\pi = \arctan(g_{\uparrow\downarrow}/g)/\pi$ for (a) $(N_\phi, N) = (3, 8)$ and (b) $(N_\phi, N) = (4, 12)$. The eigenstates are classified by $S_z = (N_\uparrow - N_\downarrow)/2$ and the total angular momentum L. The two lowest eigenenergies in each sector are displayed. The lowest eigenenergy in the sector $(S_z, L) = (0, 0)$ is subtracted from the whole spectrum. The vertical dotted lines indicate the cases of $g_{\uparrow\downarrow}/g = 0, \pm 1$.

the energy gap decreases monotonically. Slightly above $\gamma/\pi = 1/4$, the GS is replaced by a maximally imbalanced state with $S_z = N/2$, indicating a phase separation instability. The level crossing point $\gamma_{c3}(N)$ gives an estimate of the transition point. Around $\gamma/\pi \approx -0.25$ and -0.1, some energy levels show extrema, which are also related to phase transitions as we discuss next.

Figures 7(a) and 8(a) present the fidelity susceptibility $\chi_F(\gamma)$ as a function of γ/π. Here, $\chi_F(\gamma)$ is defined as

$$\chi_F(\gamma) = -2 \lim_{\delta\gamma \to 0} \frac{\ln F(\gamma, \gamma + \delta\gamma)}{(\delta\gamma)^2}, \qquad (17)$$

where $F(\gamma, \gamma + \delta\gamma) \equiv |\langle \Psi(\gamma) | \Psi(\gamma + \delta\gamma) \rangle|$ is the overlap between the GSs at the two parameter points γ and $\gamma + \delta\gamma$. This quantity measures how rapidly the GS $|\Psi(\gamma)\rangle$ changes as a function of the model parameter γ. For $\gamma < 0$, we observe two peaks in $\chi_F(\gamma)$, which indicate

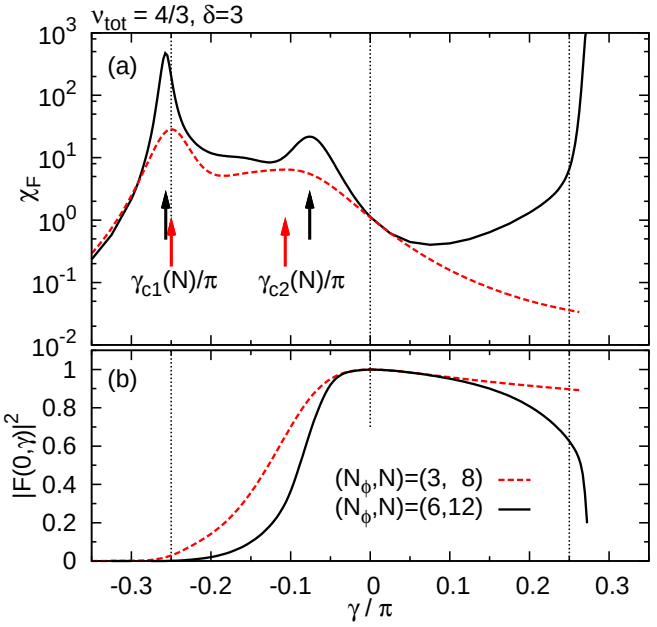

FIG. 7: (color online) (a) The fidelity susceptibility $\chi_F(\gamma)$ and (b) the squared overlap with the GS at $\gamma = 0$, i.e., $|F(0,\gamma)|^2$, for $\nu_{\rm tot} = 4/3$ and $\delta = 3$. Peak positions of $\chi_F(\gamma)$ indicated by arrows give finite-size estimates of the transition points. Vertical dotted lines indicate the cases of $\gamma = 0, \pm\pi/4$.

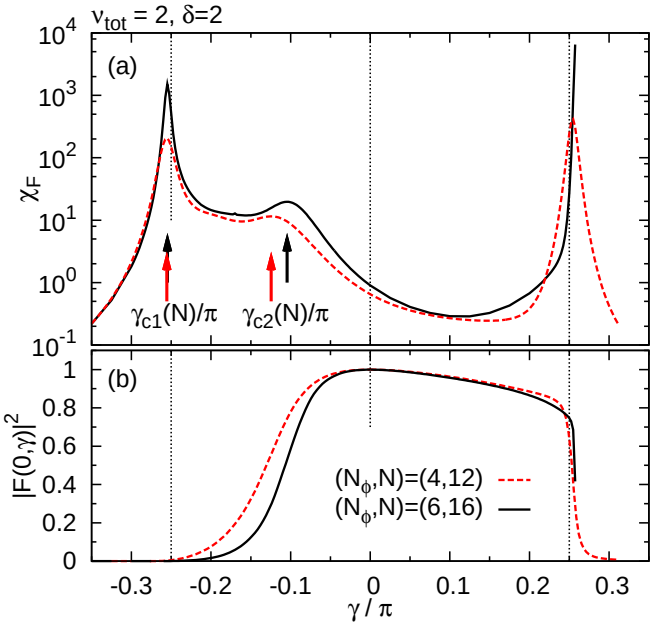

FIG. 8: (color online) (a) The fidelity susceptibility $\chi_F(\gamma)$ and (b) the squared overlap with the GS at $\gamma = 0$, i.e., $|F(0,\gamma)|^2$, for $\nu_{\rm tot} = 2$ and $\delta = 2$. Arrows and vertical dotted lines are the same as in Fig. 7.

phase transitions. The peak positions, $\gamma_{c1}(N)/\pi$ and $\gamma_{c2}(N)/\pi$ [arrows in Figs. 7(a) and 8(a)], can be used to make a finite-size estimation of the transition points. The transition point γ_{c1} is located exactly at $\gamma_{c1} = -\pi/4$ in the thermodynamic limit as discussed in the main text.

Using the data of $\gamma_{c2}(N)$ and $\gamma_{c3}(N)$ for the larger system sizes $[(N_\phi, N) = (6, 12)$ and $(6, 16)]$, we obtain the following naive estimates of the ranges of QSH phases:

$$\begin{aligned}\nu_{\rm tot} &= \frac{4}{3} : -0.076 \lesssim \gamma/\pi \lesssim 0.27 \ (-0.24 \lesssim g_{\uparrow\downarrow}/g \lesssim 1.2) \\ \nu_{\rm tot} &= 2 : -0.10 \lesssim \gamma/\pi \lesssim 0.26 \ (-0.34 \lesssim g_{\uparrow\downarrow}/g \lesssim 1.1).\end{aligned} \tag{18}$$

If we extrapolate the data of $\gamma_{c2}(N)$ to the thermodynamic limit by using a linear function of $1/N$, we obtain $\gamma_{c2}/\pi = -0.015$ and -0.044 [i.e., $(g_{\uparrow\downarrow}/g)_{c2} = -0.046$ and -0.14] for $\nu_{\rm tot} = 4/3$ and 2, respectively; these values are shifted rather largely from the estimates (the left ends of the ranges) in Eq. (18). Since we had only two data points for these extrapolations, it is possible that the extrapolations were affected by strong finite-size effects in the smaller sizes. We thus leave the precise values of $(g_{\uparrow\downarrow}/g)_{c2}$ undetermined, and show the uncertainties between the two estimates above by dotted lines in Fig. 1 of the main text.

Figures 7(b) and 8(b) shows the squared overlap with the decoupled case: $|F(0,\gamma)|^2$. We find that $|F(0,\gamma)|^2$ remains close to unity in the ranges of Eq. (18), indicating that fractional QSH states, which are well approximated by independent QH states, persist there. As in the $\nu_{\rm tot} = 1$ cases, these ranges are remarkably wide and even include the case of $g_{\uparrow\downarrow} \approx g$.

Some other exact results on the point $g_{\uparrow\downarrow} = -g$

In the main text, we derive the exact GSs with a novel paring nature at $g_{\uparrow\downarrow} = -g$. Here we explain the su(1,1) symmetry hidden behind this solution, and also present the exact calculations of the pairing amplitude and some excited states.

We start by clarifying the su(1,1) structure in the present model. We introduce

$$\begin{aligned}K_+ &= \int d\boldsymbol{r} \hat{\Psi}^\dagger_\uparrow(\boldsymbol{r})\hat{\Psi}^\dagger_\downarrow(\boldsymbol{r}), \quad K_- = K_+^\dagger, \\ K_z &= \frac{1}{2}(N_\uparrow + N_\downarrow + 2S + 1),\end{aligned} \tag{19}$$

which satisfy the su(1,1) algebra [5, 6]:

$$[K_+, K_-] = -2K_z, \quad [K_z, K_\pm] = \pm K_\pm. \tag{20}$$

The Casimir operator, which is an analogue of the magnitude of the angular momentum in su(2), is defined as

$$C = K_z^2 - \frac{1}{2}(K_+K_- + K_-K_+) = K_z(K_z - 1) - K_+K_-. \tag{21}$$

This operator commutes both with K_z and $K_\pm$. The basis vectors $|k,m\rangle$ for representing su(1,1) can be chosen to be the simultaneous eigenvectors of C and K_z:

$$\begin{aligned} C|k,m\rangle &= k(k-1)|k,m\rangle, \\ K_z|k,m\rangle &= (k+m)|k,m\rangle, \end{aligned} \tag{22}$$

where the real number $k>0$ is called the Bargmann index and m can be any nonnegative integer. In this basis, the operators $K_\pm$ play the roles of raising and lowering m by one:

$$K_+|k,m\rangle = \sqrt{(m+1)(2k+m)}\ |k,m+1\rangle, \tag{23a}$$

$$K_-|k,m\rangle = \sqrt{m(2k+m-1)}\ |k,m-1\rangle. \tag{23b}$$

In the main text, we show that the GS of the model for particle numbers $N_\uparrow = N_\downarrow = N/2$ is given by $|\Psi(N)\rangle \propto (K_+)^{N/2}|0\rangle$. Since the vacuum $|0\rangle$ is an eigenstate of C and K_z with $k = S+1/2$ and $m=0$, $|\Psi(N)\rangle$ can be identified with $|k=S+1/2, m=N/2\rangle$. The paring amplitude in $|\Psi(N)\rangle$ is thus calculated by using Eq. (23b) as

$$\begin{aligned} &\frac{1}{(4\pi R^2)^2}\langle\Psi(N)|K_+K_-|\Psi(N)\rangle \\ &= \frac{1}{(4\pi\ell^2)^2 S^2}\frac{N}{2}\left(2S+\frac{N}{2}\right) \longrightarrow \frac{\nu_{\rm tot}(2+\nu_{\rm tot})}{(4\pi\ell^2)^2}. \end{aligned} \tag{24}$$

In the last expression, we took the thermodynamic limit $N\to\infty$ while keeping $\nu_{\rm tot} = N/(2S)$ constant. This result indicates that the paring amplitude remains finite in the thermodynamic limit for any $\nu_{\rm tot}>0$ and is an increasing function of $\nu_{\rm tot}$.

We note that the SU(1,1) structure presented above is not limited to a sphere geometry but exits in a torus geometry as well; the only difference is to replace the definition of K_z by $K_z = \frac{1}{2}(N_\uparrow + N_\downarrow + N_\phi)$. The paring amplitude can also be calculated in a similar manner, resulting in the same expression as Eq. (24) in the thermodynamic limit.

Next we construct some excited states on a sphere. To this end, we introduce extended pair creation operators

$$P^\dagger_{JM} = \sum_{m_1,m_2} b^\dagger_{m_1\uparrow} b^\dagger_{m_2\downarrow}\langle S,m_1;S,m_2|J,M\rangle, \tag{25}$$

where $\langle S,m_1;S,m_2|J,M\rangle$ is the Clebsch-Gordan (CG) coefficient. This operator creates a pair of $\uparrow$ and $\downarrow$ particles with the total angular momentum (J,M). Using the expansions (11), one can show $K_+ = \sqrt{2S+1}P^\dagger_{00}$. Therefore, the GS $|\Psi(N)\rangle$ consists of $N/2$ pairs of $\uparrow$ and $\downarrow$ particles with the angular momentum $(J,M)=(0,0)$. Our basic idea is to break one such pair into a state with higher J. We start by constructing exact 2-body eigenstates for $N_\uparrow = N_\downarrow = 1$. In this case, the eigenstates are given simply by $P^\dagger_{JM}|0\rangle$ since the Hilbert space is fully decomposed in terms of (J,M). Denoting its eigenenergy by E_J, the eigenequation is written as

$$\begin{aligned} &\sum_{m_3,m_4} 2V^{\uparrow\downarrow}_{m_1,m_2,m_3,m_4}\langle S,m_4,S,m_3|J,M\rangle \\ &= E_J\langle S,m_1,S,m_2|J,M\rangle \end{aligned} \tag{26}$$

where $V^{\uparrow\downarrow}_{m_1,m_2,m_3,m_4}$ is shown in Eq. (15). Although we know that this equation should be satisfied because of the symmetry, the calculation of E_J is not simple in general because CG coefficients become increasingly complicated for larger J. Here we perform calculations for $(J,M) = (1,0)$; in this case, CG coefficients are relatively simple and their non-zero values are given by

$$\langle J,m;J,-m|1,0\rangle = \sqrt{\frac{3}{S(S+1)(2S+1)}}(-1)^{S-m}m. \tag{27}$$

Using this, the left-hand side of the eigenequation (26) is calculated as

$$\begin{aligned} &\sum_{m_3,m_4} 2V^{\uparrow\downarrow}_{m_1,m_2,m_3,m_4}\langle S,m_4,S,m_3|1,0\rangle \\ &= \delta_{m_1+m_2,0}\frac{-g}{4\pi\ell^2}\frac{(2S+1)^2}{S(4S+1)}\sqrt{\frac{3}{S(S+1)(2S+1)}} \\ &\times(-1)^{S-m_1}\sum_{m_4}\frac{C(2S,S+m_1)C(2S,S+m_4)}{C(4S,2S+m_1+m_4)}m_4 \\ &= -\frac{g}{4\pi\ell^2}\frac{2S+1}{S+1}\langle S,m_1,S,m_2|1,0\rangle, \end{aligned} \tag{28}$$

where we have used the identity

$$\begin{aligned} &\sum_{m_4}\frac{C(2S,S+m_1)C(2S,S+m_4)}{C(4S,2S+m_1+m_4)}m_4 \\ &= \frac{S(4S+1)}{(S+1)(2S+1)}m_1. \end{aligned} \tag{29}$$

The eigenenergy E_1 can then be read out from Eq. (28) as

$$E_1 = -\frac{g}{4\pi\ell^2}\frac{2S+1}{S+1}. \tag{30}$$

Excited states for particle numbers $N_\uparrow = N_\downarrow = N/2$ can be obtained by repeatedly multiplying K_+ to the two-body excited state:

$$|\Psi_{JM}(N)\rangle \propto K_+^{\frac{N}{2}-1}P^\dagger_{JM}|0\rangle. \tag{31}$$

Using

$$[H,K_+] = -\frac{g}{4\pi\ell^2}\frac{2S+1}{S}K_+, \tag{32}$$

the eigenenergy for Eq. (31) is calculated as

$$E_J(N) = E_J(2) - \frac{g}{4\pi\ell^2}\frac{2S+1}{S}\left(\frac{N}{2}-1\right). \tag{33}$$

Therefore, the excitation gap to the $J = 1$ state is obtained as

$$E_1(N) - E_{\rm GS}(N) = E_1(2) + \frac{g}{4\pi\ell^2}\frac{2S+1}{S} = \frac{g}{4\pi\ell^2}\frac{2S+1}{S(S+1)}. \quad (34)$$

Although we do not have a rigorous argument that $|\Psi_{1M}(N)\rangle$ should be the first excited state, we have confirmed that the numerical data of the neutral energy gap [the area of the circles in Fig. 5(b)] agree with this expression. This gap vanishes for $S \to \infty$, indicating that the system is gapless in the thermodynamic limit.

[1] F. D. M. Haldane, Phys. Rev. Lett. **51**, 605 (1983).

[2] G. Fano, F. Ortolani, and E. Colombo, Phys. Rev. B **34**, 2670 (1986).

[3] ARPACK developed by D.C. Sorensen, R.B. Lehoucq, C. Yang, and K. Maschhoff (URL: http://www.caam.rice.edu/software/ARPACK/).

[4] N. Read and E. H. Rezayi, Phys. Rev. B **59**, 8084 (1999).

[5] For an introduction to the su(1,1) algebra, see, e.g., M. Novaes, Rev. Bras. Ensino Fis. **26**, 351 (2004).

[6] A similar algebraic structure has also been discussed in studies of spinor Bose-Einstein condensates. See M. Ueda and M. Koashi, Phys. Rev. A **65**, 063602 (2002).